The Planetary Science Journal, 4:21 (12pp), 2023 February https://doi.org/10.3847/PSJ/acaddb

Highly Resolved Topography and Illumination at Mercury's South Pole from MESSENGER MDIS NAC

Stefano Bertone[1,2,3], Erwan Mazarico[2], Michael K. Barker[2], Matthew A. Siegler[4], Jose M. Martinez-Camacho[4,5], Colin D. Hamill[6], Allison K. Glantzberg[7], and Nancy L. Chabot[7]
[1] Center for Research and Exploration in Space Science and Technology, University of Maryland Baltimore County, 1000 Hilltop Circle, Baltimore, MD 21250, USA
stefano.bertone@nasa.gov
[2] NASA Goddard Space Flight Center (GSFC), Code 698, 8800 Greenbelt Road, Greenbelt, MD 20771, USA
[3] INAF, Astrophysical Observatory of Torino, Via Osservatorio 20, 10025 - Pino Torinese (TO), Italy
[4] Planetary Science Institute, 1700 East Fort Lowell, Suite 106, Tucson, AZ 85719, USA
[5] Southern Methodist University, Roy M. Huffington Department of Earth Sciences, 6425 Boaz Lane, Dallas, TX 75205, USA
[6] Purdue University, Department of Earth, Atmospheric, and Planetary Sciences, 550 Stadium Mall Drive, Lafayette, IN 47904, USA
[7] Johns Hopkins University Applied Physics Laboratory, 11100 Johns Hopkins Road, Laurel, MD 20723, USA
Received 2022 October 3; revised 2022 December 19; accepted 2022 December 20; published 2023 February 2

Abstract

Mercury's south polar region is of particular interest since Arecibo radar measurements show many high-reflectance regions consistent with ice deposits. However, current elevation information in Mercury's southern hemisphere is not sufficient to perform detailed modeling of the illumination and thermal conditions at these radar-bright locations and to constrain properties of the volatiles potentially residing there. In this work, we leverage previously existing elevation maps of Mercury's surface from stereo-photogrammetry at 665 m pix^{-1}, Mercury Dual Imaging System Narrow Angle Camera images, and Shape-from-Shading tools from the Ames Stereo Pipeline, to provide the first high-resolution topographic maps of the south pole with a resolution of 250 m pix^{-1} poleward of 75°S. We show that the increased resolution and level of detail provided by our new elevation model allow for a more realistic recovery of illumination conditions in Mercury's south polar region, thus opening the way to future thermal analyses and for the characterization of potential ice and volatile deposits. We compare both the old and new topographic models to the Mercury Dual Imaging System Narrow Angle Camera images to show the higher level of fidelity with our products, and we assess the improved consistency of derived permanently shadowed regions with reflectance measurements by Arecibo's antennas.

Unified Astronomy Thesaurus concepts: Mercury (planet) (1024); Remote sensing (2191); Planetary polar regions (1251); Planetary surfaces (2113); Surface ices (2117)

1. Introduction

Mercury's south polar region is of particular interest since Arecibo radar measurements show many high-reflectance regions consistent with ice deposits (Harmon et al. 2011; Chabot et al. 2018). Detailed modeling of the illumination and thermal conditions at these radar-bright locations would allow the first constraints on the volatiles potentially residing there. Where detailed topographic models of airless bodies are available (e.g., Zuber et al. 2012; Preusker et al. 2016; Smith et al. 2017; Glaser et al. 2018; Barker et al. 2021), they have been used as the basis for geophysical and geological studies (e.g., Susorney et al. 2017) and to compute illumination conditions and temperatures at or near the surface (e.g., Paige et al. 2010; Mazarico et al. 2011; Glaser et al. 2014; Schorghofer et al. 2016; Fisher et al. 2017; Mazarico et al. 2018; Gläser & Gläser 2019; Schorghofer et al. 2021; Landis et al. 2022; Siegler et al. 2022), thus characterizing the optical and thermophysical properties of surface compounds, and setting constraints on their evolution. In particular, at Mercury, the north polar region was studied first given detailed elevation information from the Mercury Laser Altimeter (MLA) was available. Early simulations of the north polar region's illumination conditions and thermal environment were described in Neumann et al. (2013) and in Paige et al. (2013), using the first year of MLA data. More accurate simulations, based on the complete MLA data set, were first published in Chabot et al. (2018b), and more recently by Gläser (2022). Other studies (Deutsch et al. 2016; Rubanenko et al. 2018; Susorney et al. 2021) have also focused on the north polar region leveraging the MLA elevation models (see, e.g., Zuber et al. 2012; Hamill et al. 2020; Barker et al. 2022), in part because no reliable high-resolution elevation data for the southern polar region are available.

Because of the very eccentric orbit of the MErcury Surface, Space ENvironment, GEochemistry and Ranging (MESSENGER; Solomon et al. 2008) spacecraft, with periapsis over northern latitudes, its observations of southern regions were limited due to large spacecraft distances from the planet. For instance, no MLA ranges to the surface are available below 10° south (see, e.g., Zuber et al. 2012), so that elevation information in the southern hemisphere is limited to what can be recovered from the Mercury Dual Imaging System (MDIS; Hawkins et al. 2007) supplemented by radio occultations (Perry et al. 2015). Past studies have used stereo-photogrammetry (SPG) with MDIS data to produce elevation maps of Mercury's surface, both global ones (Becker et al. 2016; USGS in the following) at 665 m pix^{-1} and localized ones focusing on several Mercury quadrangles (Preusker et al. 2018). However, this technique is difficult to use in polar regions, where strong shadowing hinders SPG and few stereo pairs are available. Moreover, the method employed

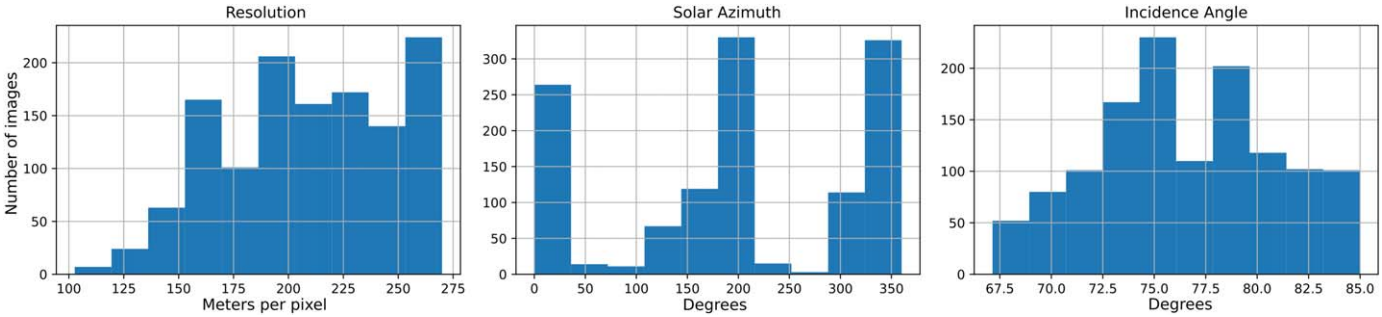

Figure 1. Properties of our selection of NAC images for SfS processing. All quantities refer to the center of the NAC images, each ∼200 km wide (varying with spacecraft distance to the surface and with the angle of observation). The range of image resolutions and the variety of solar azimuths allow for a robust recovery of elevation information using SfS.

by Becker et al. (2016) could not resolve terrain elevation at latitudes poleward of 87°S, where many large permanently shadowed regions (PSRs) and radar-bright regions are located. As such, it is currently not possible to produce the highly resolved illumination and thermal maps needed to understand the presence and nature of most south polar bright deposits, in order to extend previous studies such as Chabot et al. (2018) and Rivera-Valentin et al. (2022). With the ESA mission BepiColombo (Benkhoff et al. 2010) still several years away from entering orbit, it is important to further exploit MESSENGER's extensive data sets to retrieve additional information about the planet, for both geophysical analysis and preparation for the upcoming mission. In this study, we use an approach called photoclinometry (Horn 1970), or Shape-from-Shading (SfS), to provide higher-resolution topographic maps of the south pole. In particular, we apply tools available within the Ames Stereo Pipeline (ASP; Alexandrov & Beyer 2018; Beyer et al. 2018, 2021a) to MDIS Narrow Angle Camera (NAC) images, to recover topography with a resolution of 250 m pix^{-1} at latitudes poleward of 75° South (an area covering $\sim 1.3 \times 10^6$ km^2). That latitude was chosen as it includes the large majority of PSRs and bright deposits from Chabot et al. (2018). Our results are a key step toward advancing our knowledge of volatiles in Mercury's south polar region. The increased resolution and level of detail provided by our new topographic model opens the door for realistic simulations of illumination and thermal conditions in Mercury's south polar region and will allow new constraints on the nature and history of volatiles on Mercury, for which intercomparison between the two poles can be particularly informative.

In Section 2, we present the data sets, tools, and methods used in our analysis. We validate our approach and present our novel topography maps in Section 3. We compare selected NAC images with realistic renderings based on both the existing USGS model and on our new topography model. Finally, we compare the PSRs inferred from both models to Arecibo's radar brightness measurements and to previous estimates of terrain illumination to highlight the increased predictive capability of our product.

2. Data, Software, and Methods

We use a selection of MDIS NAC images (see Section 2.1) and several routines within the publicly available ASP software package (see Section 2.2) to recover terrain elevation poleward of 75°S with a resolution of 250 m pix^{-1}. While the core of our analysis is the ASP `sfs` routine, several pre- and post-processing steps are required to achieve an accurate and reliable result.

2.1. MDIS NAC

Due to the considerable distance between the MESSENGER spacecraft and the surface above Mercury's south polar region (up to 15,000 km), well outside of MLA's ranging capability, we base our topography recovery on MDIS NAC images and on SfS. Of the ⩾270,000 geolocated MDIS images available on the NASA Planetary Data System for the whole planet, we selected the subset of NAC images with a pixel scale better than 270 m pix^{-1}, an off-nadir angle ⩽45°, an incidence angle ⩽85° (so that the image is taken on the dayside of Mercury), and a ⪆20% overlap with the latitudes of interest. Such criteria guarantee that no image with extreme illumination conditions or poor resolution enters our analysis and degrades the resulting topographic map. For the same reason, we also screen out a few images with bad or saturated pixels. The main characteristics of our final data set of ∼1300 NAC images are shown in Figure 1. SfS works best when multiple images per scene are available, sampling a wide range of solar azimuths. Even though our selection shows two preferred modes at 0° and 180° Sun azimuth (similar to what is present in the full NAC database at these latitudes), the distribution of illumination angles is sufficiently broad for the SfS processing detailed in Section 2.2.

2.2. ASP and SfS Processing

In recent years, SfS has been successfully applied to many terrestrial bodies (see, e.g., Gaskell et al. 2008; Jorda et al. 2016; Fassett 2016; Alexandrov & Beyer 2018; Barnouin et al. 2020). In this method, the terrain slope is inferred from the shading differences in images caused by variations in illumination and observation geometry. Topography is then obtained from the reconstructed slopes.

SfS has been shown to recover topography at or near the native image pixel scale (Alexandrov & Beyer 2018, and references therein), so we use ASP to build an elevation model with a pixel scale of 250 m pix^{-1}, which is close to the upper end of resolutions available in our selection (see Figure 1). Since processing topography for the whole target latitudes at once would not be computationally feasible, we split Mercury's polar cap (up to a square region enclosing 75° S) in ∼200 km wide square tiles (in stereographic projection, see Figure 2), overlapping by 20% on each side and covering the whole area of interest. We developed a tool based on publicly available geographic and geometric python libraries (e.g., *shapely, fiona, pyproj, sklearn*, and *geopandas*) to automate the usually cumbersome task of selecting an optimal set of images while ensuring both full surface coverage and that multiple images with different illumination angles overlap at each point on the

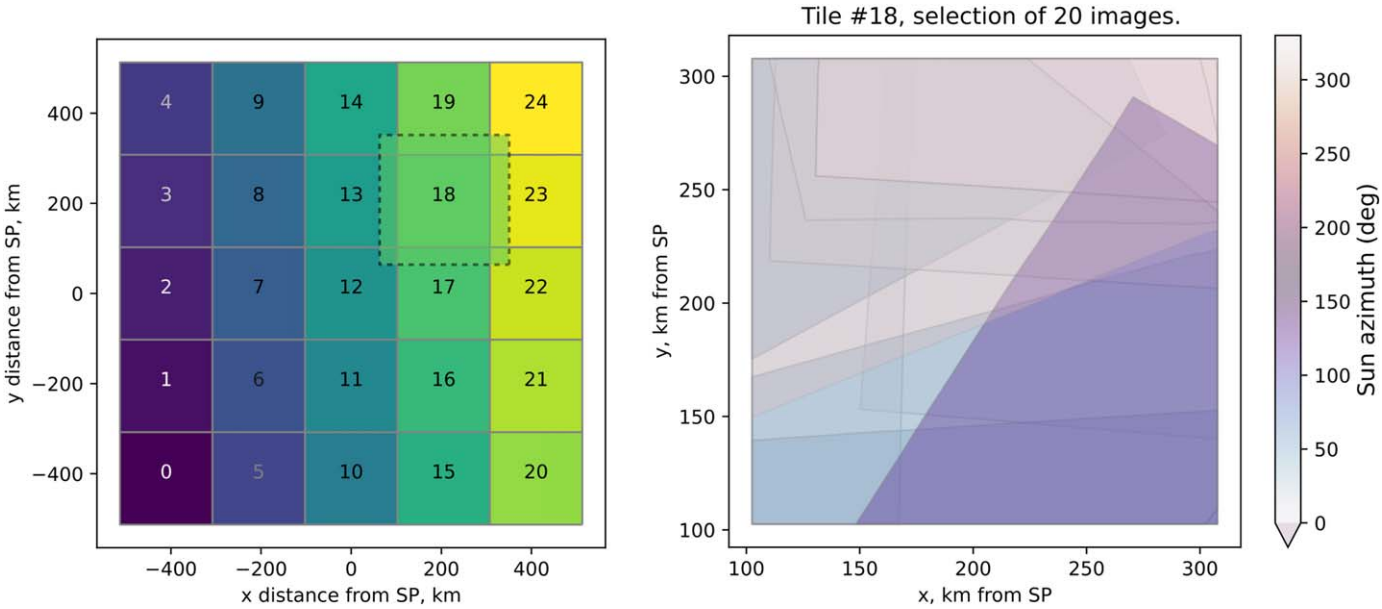

Figure 2. Left: stereographic projection of the reconstructed region showing our partition in overlapping square tiles (200 km on a side, with 20% overlap as shown by the dashed line centered on tile 18); right: coverage of square tile #18 by a selection of 20 MDIS NAC images, represented by geolocated polygons for lighter computations, optimizing the Sun's azimuthal and spatial coverage.

surface of the tile. We perform this step on simple polygons covering the same projected footprint as the NAC images (instead of importing and processing the actual images), thus avoiding heavy computations, and time and memory requirements. We verified that the use of 20 NAC images per tile is a good compromise between maximizing the geographic and azimuthal coverage and minimizing the processing time and the risk of misalignment between images (which grows rapidly with a larger data set). We checked our automated selection against manual image selections operated via the USGS Pilot tool (Bailen et al. 2015) and found it satisfactory. We also prepared diagnostic tools to visually (see Figure 2) or statistically verify the tile coverage and azimuth distribution. When needed, individual images are manually added or removed from the selection, e.g., to cover a specific area or illumination angle, or because of localized defects or extended shadowed areas in the images. We then process the selected images using the USGS Integrated Software for Imagers and Spectrometers (ISIS3; Laura et al. 2022) package to calibrate and geolocate them. We finally use the ASP `mapproject` tool to project the selected images onto the a priori digital elevation model (DEM). The latter is extracted from Becker et al. (2016, see Figure 3) to match the extent of the chosen tile and is interpolated to the target resolution of 250 m pix^{-1}. ISIS3 cameras, projected images, and a priori DEM are then fed to the `bundle_adjust` ASP tool, which improves the consistency of their alignments. The bundle-adjusted image network is then realigned to the a priori DEM via the `pc_align` tool. The refined cameras are then passed along with the a priori DEM as input to the ASP `sfs` tool, which adjusts a set of parameters (including the elevation model and the camera position and orientation) by minimizing differences between the measured pixel intensities and simulated intensities computed by ray tracing with the a priori DEM. The solution is then iterated to convergence (∼10–15 iterations). To regularize the solutions, ASP allows to set up constraints on the "smoothing" and on how much the solution is allowed to stray away from the initial model. We use the ASP `sfs` tool assuming a Lunar–Lambertian light reflection law (McEwen 1996), which has been shown to perform well on a variety of airless bodies (Gaskell et al. 2008). We apply shadow thresholds to the input images to exclude shadowed pixels. Besides estimating new DEM values, we also allow `sfs` to refine camera positions. The cost function minimized by `sfs` (Alexandrov & Beyer 2018) is then

$$\int\int \sum_k [I_k(\phi(x, y)) - T_k A(x, y) R_k(\phi(x, y))]^2 + \mu \nabla^2 \phi(x, y)||^2 + \lambda[\phi(x, y) - \phi_0(x, y)]^2 dxdy, \quad (1)$$

where $I_k(\phi)(x, y)$ represent intensity values from the k-th camera image projected and interpolated at 3D points from the current best-fit DEM terrain $\phi(x, y)$, T_k is the k-th image exposure, $A(x, y)$ is the per-pixel albedo (that we keep fixed at 1), $R_k(\phi)(x, y)$ is the reflectance computed from the terrain for the k-th image, $\nabla^2\phi(x, y)$ is the sum of squares of all second-order partial derivatives of ϕ, $\mu > 0$ is a smoothing term (a smaller μ will result in more detail but also in more artifacts), and $\lambda > 0$ determines how close the solution should stay to the a priori DEM ϕ_0 (smaller λ allows for a more aggressive optimization but elevation estimates may stray too far from the a priori; Beyer et al. 2021b). Based on our experience and the results of our systematic experiments at Mercury's poles, we set these weighting factors to $\mu = 2.5$ and $\lambda = 10^{-6}$, respectively.

For each terrain tile and batch of preselected images, we mainly follow the prescriptions of Beyer et al. (2021b), but we slightly adapted our detailed processing with the following steps to ensure a robust result. First, we project a larger selection of ∼50 overlapping images (including our core selection of 20 images for SfS) on an extended DEM (beyond the terrain tile, to maximize overlapping regions among images). Second, we bundle-adjust all projected images, then compute a single translation to realign them to the a priori DEM and pass the resulting camera corrections as input to

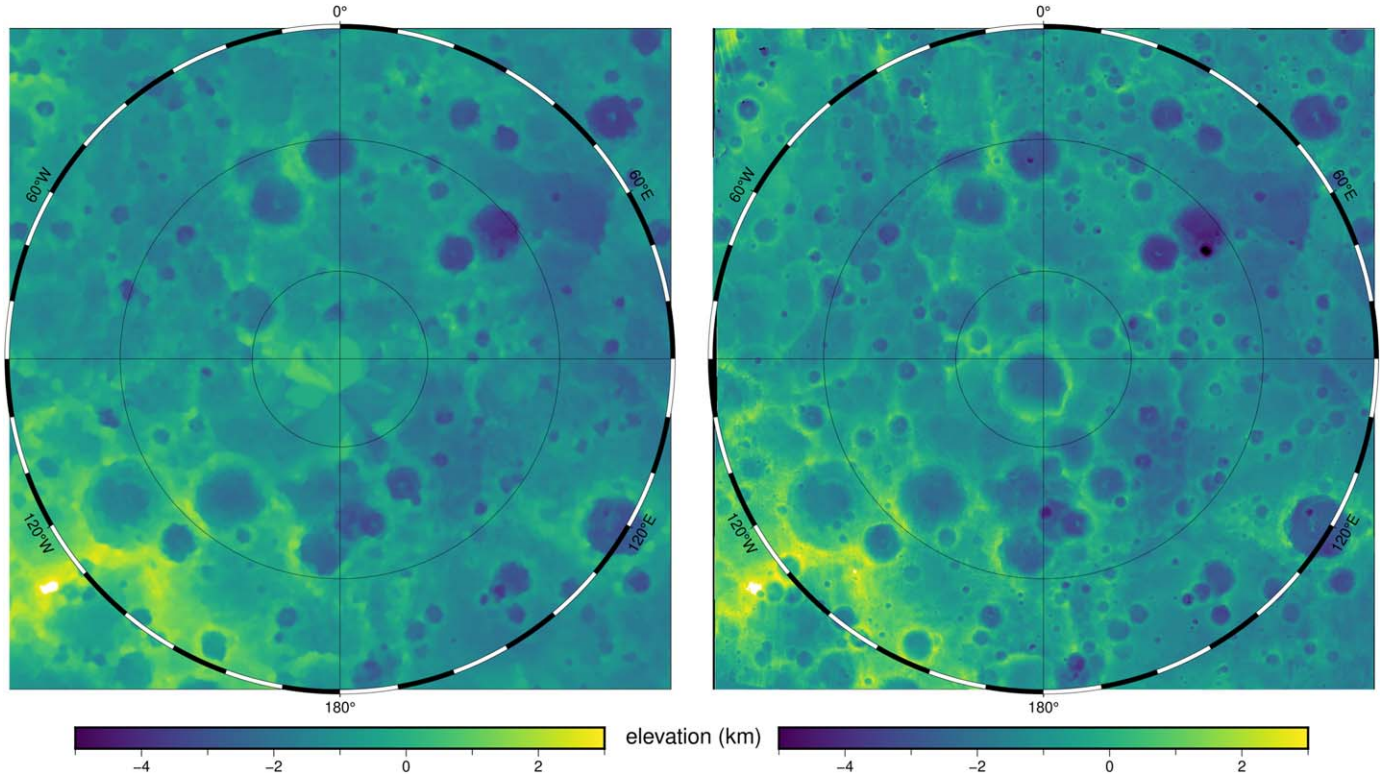

Figure 3. The current USGS stereo elevation model (Becker et al. 2016) at 665 m pix^{-1} (left), that we use as a priori for our study, and our new 250 m pix^{-1} SfS elevation model (right) for Mercury's south pole region. Differences between the two models are shown in Figure 5(a). Latitude circles represent distances of 5°, while black-and-white intervals indicate longitude steps of 10°.

`sfs`. Then, we perform SfS at low resolution (500 m pix^{-1}) starting with one of the 20 selected images and then adding one image at a time, iteratively updating camera corrections from the previous step. Finally, we perform SfS at target resolution (250 m pix^{-1}) with the 20 selected images, using the improved camera positions as a priori and reestimating both terrain and cameras. These steps result in a set of terrain tiles with improved elevations. However, while SfS performs well in recovering local features, it lacks the large-scale control of laser altimetry or stereo reconstruction. For this reason, we carefully align the resulting terrain tiles to Becker et al. (2016) and, through a global rigid transformation alignment, to the overlapping regions. We then blend the tiles into a seamless mosaic using ASP's suite of tools, resulting in the elevation map shown in Figure 3 (right).

3. Results

We show in Figure 3 (right) our new 250 m pix^{-1} elevation map of Mercury's south pole, covering the whole region below 75°S and resulting from the SfS processing presented in Section 2.2. Most crater rims are clearly recognizable, as well as many features down to image resolution. Large-scale features, such as the high elevation region at 70–75°S and 130–150°W (lower left in Figure 3), are visible both in our model and in Becker et al. (2016; see Figure 3, left), which we used as a priori.

While we significantly improve the elevation model for the whole region, we especially provide the first elevation models poleward of 85°S, where the USGS map relies on interpolation to fill much of this region (see Figures 3 and 4). Differences between the two models are shown in Figure 5(a).

The Chao Meng-Fu crater (CMF; 87.3° S, 132.4° W) required additional manual processing due to the minimal illumination available in (mostly long exposure) NAC images and nonexistent a priori elevation information. After experimenting with various `sfs` settings and processing methodologies in that crater, we chose to manually adjust the `sfs` output DEM within the `Blender` software package (Blender Online Community 2018), in order to best ensure consistency between the rendered DEM and the few long-exposure images available. In particular, we manually carved portions of CMF (e.g., 100–180° *W*) from the initial `sfs` interpolation output, to reflect the lack of illumination in all available NAC images, and to enforce a more physical radial profile that the `sfs` tool could not account for. The improved DEM was then fed as input to `sfs` for a final iteration before being aligned and blended with other tiles.

Figure 4 shows a comparison between the slopes derived from our elevation model and from the USGS model using the `gdaldem slope` tool. One can appreciate the increased level of detail over the whole region, due both to the increased resolution and from our use of a greater number of MDIS NAC images. Hill-shading of elevation maps is another common way of highlighting terrain features. In Figure 6 we compare the hill-shaded versions of our DEM (computed by the `ASP hillshade` tool) with the USGS DEM. While the main craters are recognizable in both versions, ours shows them with consistent, clear rims and a higher level of detail, as expected. Some "striping" is still visible in limited areas of our DEM, due to limitations in the illumination conditions available in NAC images, and of residual imperfections in their alignment. However, this mainly occurs outside of the 75°S circle and of our region of interest for the characterization of potential

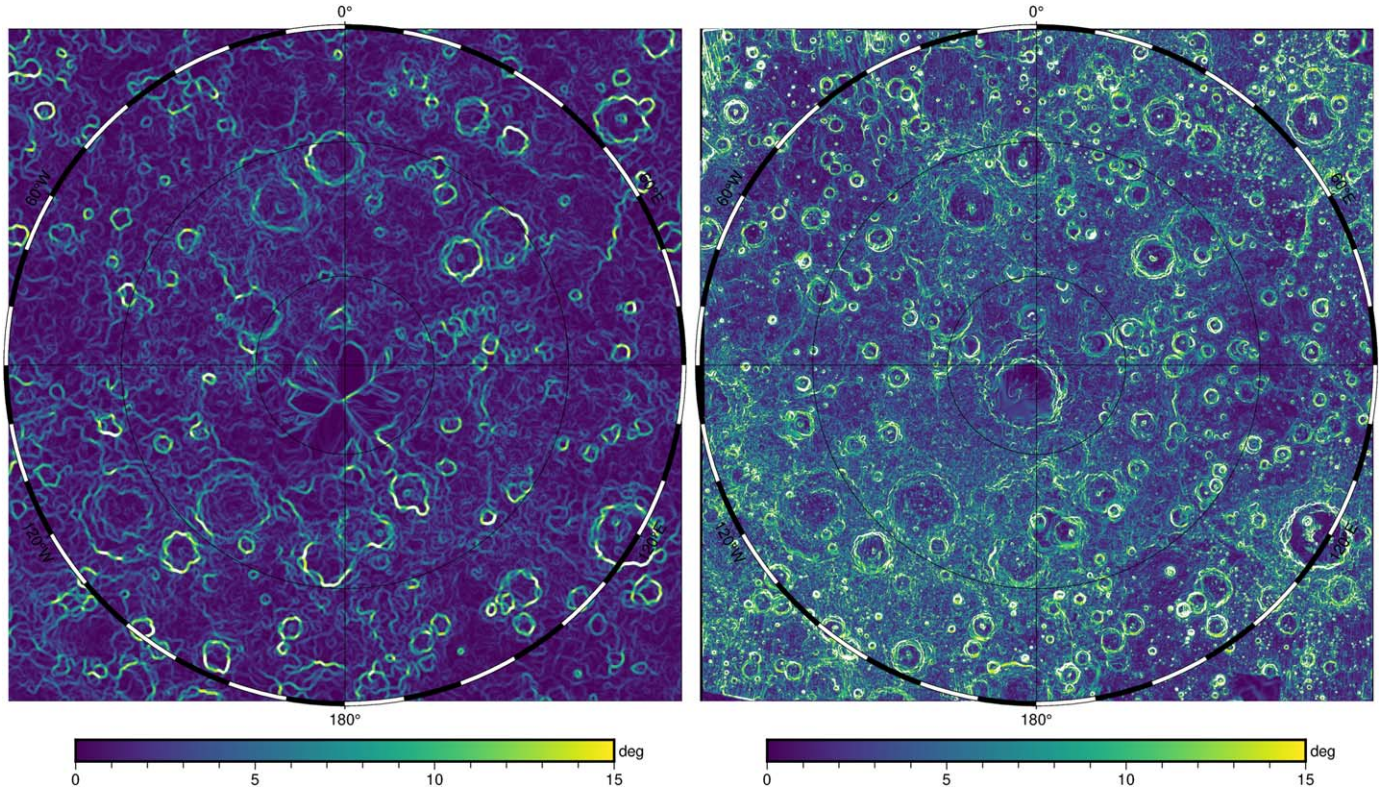

Figure 4. Slopes computed from the USGS stereo elevation model (Becker et al. 2016) at 665 m pix^{-1} (left) and from our new 250 m pix^{-1} model based on Shape-from-Shading (right). Our new model shows many more detailed features and smaller craters, which are key to determining reliable illumination and thermal conditions at the surface. See Figure 3 for additional details.

volatile deposits. The 100–180° W portion of CMF also shows smooth interpolated regions in both Figures 4 and 6, as expected due to lack of data.

Terrain within PSRs cannot be constrained by regular NAC images. Given that no MLA measurements are available to recover terrain elevation in shadowed south polar areas, we produced two versions of our improved terrain maps: one where PSRs are simply interpolated by `sfs` from the neighboring terrain, and another one where we assume a nearly axisymmetric radial profile for well-defined craters in order to fill in their PSRs with information from their sunlit portions. While the latter interpolation strategy is in a way "more processing artifacts are sometimes introduced in both maps. Each user should assess which product best fits their needs, while keeping in mind that any of the topography derived or interpolated for PSRs (e.g., based on the surrounding sunlit topography or enforced to fit prior knowledge) is not directly observed by MDIS. To identify (and eventually exclude) these less robust regions, we will also distribute a mask covering all areas of the map with no available data.

3.1. Comparison and Evaluation of the Effective Resolution

In Figures 3, 4, and 6, we provided an overview of our new terrain model. We will later show (see Figure 7 and details in Section 3.2) that rendering our new DEM provides a much closer match to NAC images of Mercury's south polar region than previous models. In addition to this visual validation, we provide here several quantitative quality metrics.

We carefully checked our results for potential artifacts or inconsistencies, both internally or against NAC images or the USGS DEM, which we used as large-scale reference. Direct differences against the USGS DEM (Becker et al. 2016) do not reveal any evident misalignment or broad-scale biases or elevation discrepancies (see Figure 5), except at the outer limit of our model (around 75°S/45°W) and below 85°S, where we recover the morphology of the CMF region for the first time. As expected, Figure 5 shows that differences between the USGS and our elevation map are due to the increased level of detail in all areas (inside craters, but also on plains and rims). As described in Section 2.2, the "tiles" composing our DEM have a 20% overlap with neighboring tiles, which we use to align them to each other, and also to evaluate the internal consistency of our model. The overall rms of overlap differences among our tiles is 280 m, which we take as one measure of the model "effective" resolution. However, overlap differences vary regionally, with median elevation differences up to several tens of meters, and standard deviations in the range 150–460 m, as shown by Figure 5. While this confirms the overall lack of large-scale biases in our model, residual elevation differences at overlaps can be due to imperfections in the reconstruction of one or both tiles, an imperfect alignment of the tiles, horizontally and/or vertically, or simply to using different images. The total altitude range in our DEM is ∼6 km, consistent with previous estimates at the same latitudes on Mercury. The elevation distributions of the two DEMs are also similar, peaking around −1 km as shown in Figure 5.

A visual inspection of our DEM shows the size of the minimum resolvable terrain feature to be ∼500–700 m, corresponding to 2–3 × the pixels size. In the case of the USGS DEM, we find a minimum resolvable feature size of 4–5 km, a bit larger than this ratio; this is potentially due to the lower density of stereo match points in the polar regions before

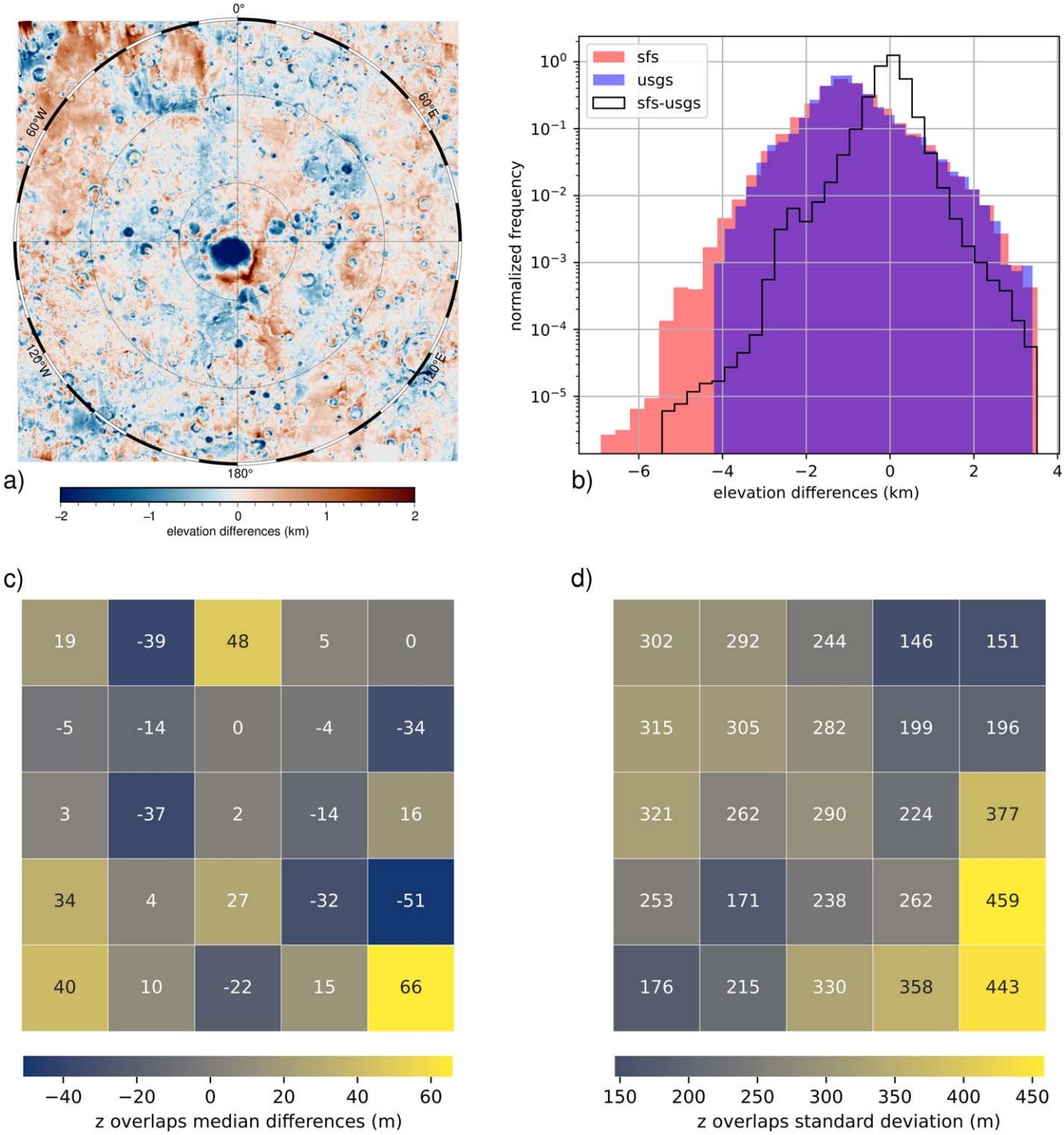

Figure 5. Differences between our DEM and the USGS one (a) mainly show the different level of detail and no shifts or biases between the two elevation maps. Close to the south pole, large differences are expected due to interpolation in the USGS map and indicate large improvements in our model. Elevation histograms (b) show that both DEMs follow similar distributions and peak at the same elevation of −1 km. The missing "low elevation tail" from the USGS histogram is also related to its missing CMF region. Their differences (black curve) do not show any evident bias. Medians (c) and standard deviations (d) of overlap Z errors among our DEM's tiles show agreement among most tiles within some tens of meters, with a spread consistent with the expected resolution of a few hundred meters.

the DEM is created at its fixed 665 m resolution. As an additional measure of the topographic information content in our DEM, we compute the power spectral density (PSD) of terrain elevation. Figure 8 shows that the overall PSD of our DEM (blue) is consistently greater than in the USGS DEM (orange), thus confirming the visual impression of a more resolved map. The USGS DEM PSD only takes over at baselines larger than 200 km, which is the size of each SfS tile. The PSD in Figure 8 is consistent with the visually estimated resolution for our DEM (shadowed blue region just near a slope

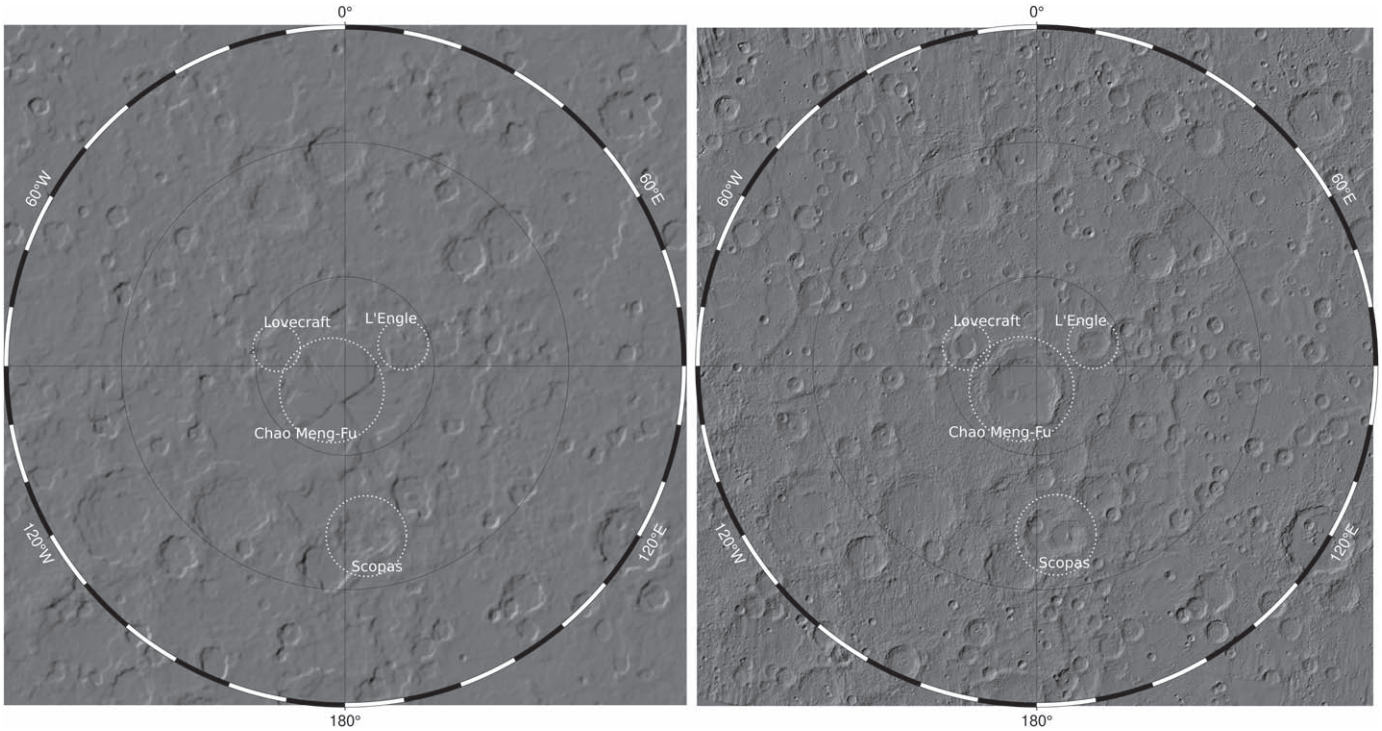

Figure 6. The additional level of detail in our new elevations model (right) is highlighted by these hill-shaded maps (Sun azimuth 300° and elevation 20°) with respect to Becker et al. (2016; left). See Figure 3 for additional details. We label the location of several polar craters harboring radar-bright areas (see Harmon et al. 2011; Chabot et al. 2018).

break in the spectrum). The spectrum for the USGS DEM is more complex, likely due to the interpolation required to obtain a uniformly gridded map from the scattered stereo match points. That degradation effect is roughly consistent with our visual estimate (shadowed orange region), with a lot of the signal at baselines close to 1–3 km potentially smoothing artifacts of interpolation (a flatter PSD due to smoothing would be closer to white noise behavior, with no actual topographic information content).

3.2. Illumination Conditions at Mercury's South Pole

The increased resolution and level of detail provided by our new elevation model open the door to realistic computations of illumination and thermal conditions at Mercury's south polar region, and specifically for the analysis of potential ice and volatile deposits, thus extending the study by Chabot et al. (2018).

To demonstrate the potential of our new model, we use here a cython interface (see Potter et al. 2022) to the publicly available CGAL library (The CGAL Project 2022) to render both our new elevation model and the USGS model with direct sunlight at selected locations. We then compare both renderings to MDIS NAC images of the same regions, which also serve as additional validation of our results. We focus on regions where bright deposits have been previously observed and where our DEM significantly differs from the USGS one (see Figure 5).

Figure 7 shows the increased potential of our new model to realistically recover illumination conditions within several craters. From top to bottom, we focus on the following regions, that we identify by the main crater: Lovecraft (86.24° S, 73.82° W), CMF (87.3° S, 132.4° W), Scopas (81.26° S, 185.29° W), L'Engle (86.63° S, 290.38° W), and Scopas again (but under different illumination conditions). Both DEMs have been interpolated and rendered at a resolution of 500 m pix^{-1} for this analysis. The increased consistency in both resolution and local details is especially visible close to the main south pole craters, where the USGS model was poorly or not resolved. In particular, rendering results for the CMF crater are particularly impressive, given the very little information available from a few long-exposure images, which are less resolved and more laborious to process. By enabling the simulation of any illumination condition at a higher resolution than before, our model opens the way to more detailed analysis of the geological and geophysical properties inside this large polar crater. However, as detailed in Section 3, a large portion of the crater's floor is never illuminated, so that only an upper bound to its elevation can be inferred from available data. Even nearer the equator, such as Scopas crater, our model shows more realistic surface shadows, which are beneficial for future studies of the whole region.

We note that our DEM is only reliable outside of PSRs, so that despite overall major improvements, residual slope and illumination artifacts can still be found in the PSRs and in the adjacent regions (see, e.g., L'Engle crater in Figure 6). Residual "striping" can also be sometimes visible outside of PSRs and under specific illumination conditions. This is typical of SfS when dealing with a limited range of available solar azimuths at a given location. Such artifacts could potentially be mitigated to some extent with the use of more images at the expense of longer processing times. However, as described above, we already tried to maximize the range of Sun azimuths with the selected images and therefore any additional benefit would be relatively small and would likely not warrant the longer processing time. Moreover, due to the regional extent of our

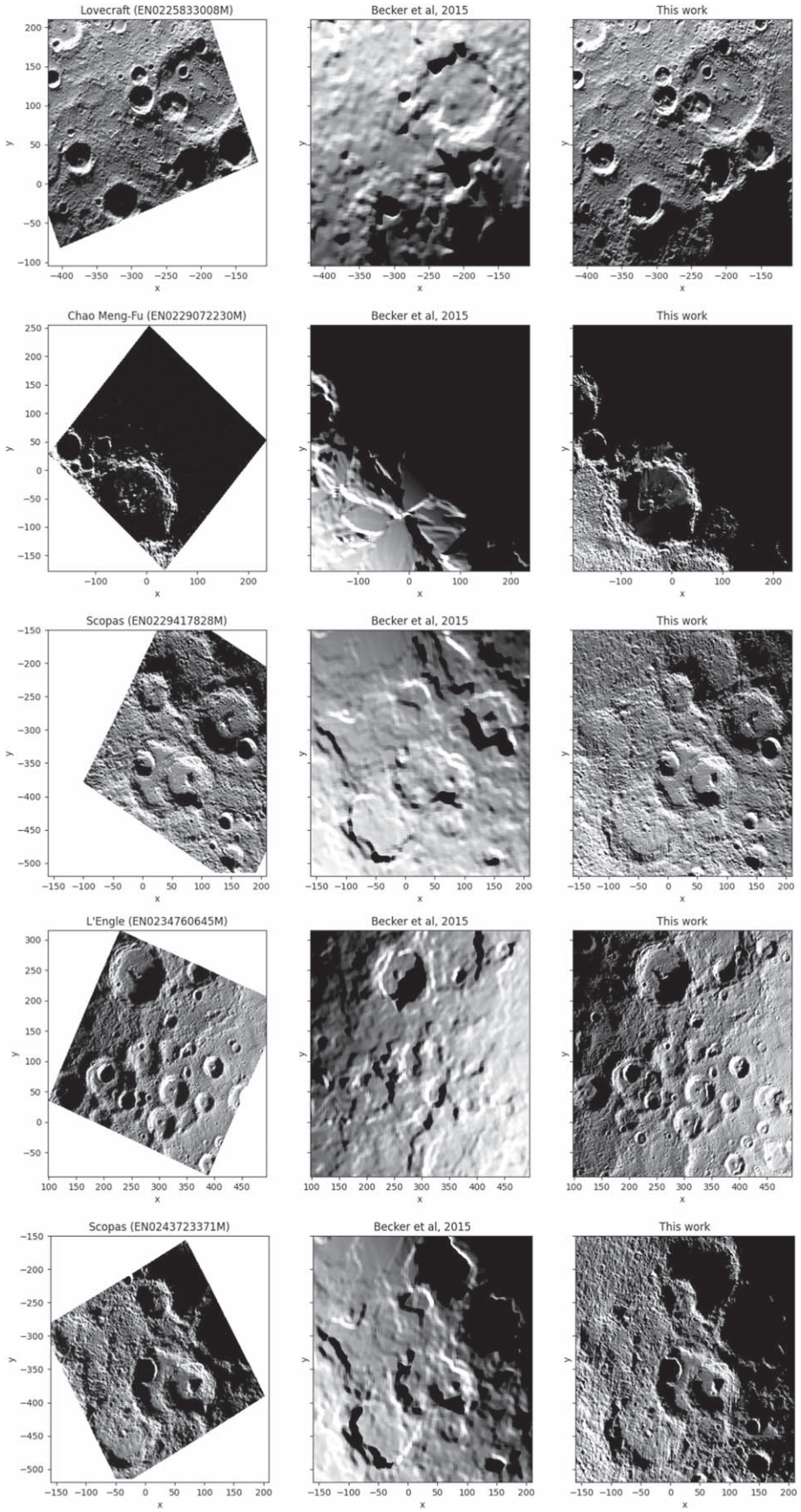

Figure 7. List of MDIS NAC images at several south polar locations (left) along with their rendering with direct Sun illumination based on the USGS DEM (Becker et al. 2016, center) and with our new DEM (right). Our model shows a much better consistency with the NAC images, when consistently illuminated, which validates our product and highlights potential uses for future studies.

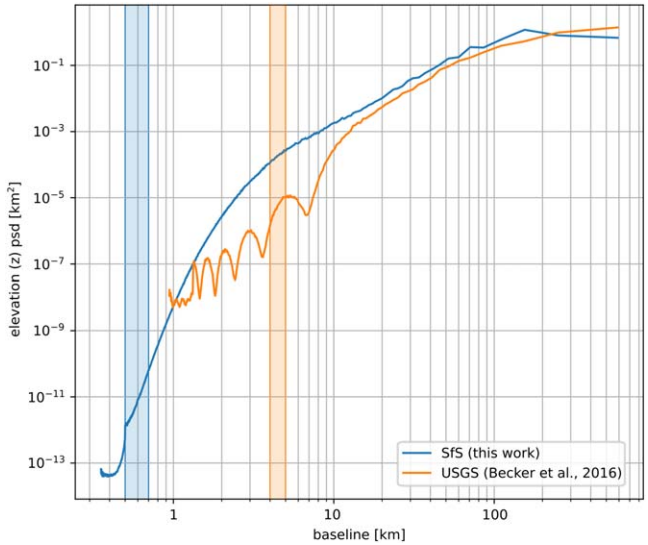

Figure 8. Comparison of the power spectral density (PSD) of the terrain elevation for both our DEM and the USGS DEM. The overlaid shadowed regions indicate the range of our visual estimates for the effective resolution of each DEM.

DEM, not every local feature can be thoroughly refined within this study, leaving this task to future analyses of specific sites.

Rendering from a reliable DEM also allows an increase in the time coverage and resolution available from remote imaging, by modeling terrain illumination at any epoch and rate as needed. In turn, this allows us to get a homogeneous evaluation of which regions receive more or less sunlight over the whole year, thus providing a proxy for warmer or colder areas on airless bodies. With that in mind, we then illuminate both DEMs over a full Mercury solar day (∼176 Earth days), with the same 12 hr time steps and the same interpolation at 500 m pix^{-1} (for computational reasons given the scope of this paper). We show in Figure 9 several characteristic phases along the solar cycle at Mercury's south pole, obtained by illuminating the whole region under several different angles. This figure emphasizes how our new DEM enables a homogeneous coverage of the whole Mercury's south pole. This is an important feature for future comprehensive illumination and thermal analyses of the polar region.

Differences between ours and the USGS DEM (shown in Figure 5) occur in the bright areas identified by the analysis of Arecibo's radar observations from Harmon et al. (2011) and with regions of persistent shadow based on the maximum illumination available on NAC images (see results from Chabot et al. 2018). In Figure 10, we compare the latter with predicted permanent shadow from both DEMs. For our rendering-based PSRs, we set two different shadow thresholds based on the average Sun flux received over a Mercury solar day. We prefer mapping the average flux rather than the maximum flux, as the former is a better proxy for subsurface temperatures and ice sublimation rates of volatiles to which ground-based radar is sensitive to (see Schorghofer et al. 2021). Regions that are PSRs in Chabot et al. (2018) and modeled here to receive an average flux of <1 W m^{-2} (or <50 W m^{-2}, to account for elevation uncertainties at or near the PSRs) are marked in yellow (or blue). Red regions are PSRs only for Chabot et al. (2018), while black regions are only predicted as PSRs by the DEM-based modeling (with an average flux <50 W m^{-2}). Our DEM shows a much higher level of consistency with Chabot et al. (2018) than the USGS rendering, with discrepancies (red/black regions) mostly limited to small-scale features. Consistency at and around CMF is again especially good, paving the way for more detailed studies in this previously mostly inaccessible region.

Using the average illumination as a rough proxy for the average temperature reached by the surface, we also check preliminary consistency of radar-bright regions from Harmon et al. (2011) with PSRs from our model. Since radar-bright regions are believed to be related to ice and volatile deposits, they could only survive in PSRs at or close to the surface. In Figure 11, we overlay radar-bright deposits to the average flux received at the surface from the Sun over a full solar cycle. Again, we mark in yellow (or blue) radar-bright deposits falling inside PSRs predicted by our renderings at <1 (or <50) W m^{-2}, and in orange those falling outside them. One clearly notices the increased consistency between radar-bright and permanently shadowed (likely cold) regions when using our SfS elevation model rather than the USGS one. Enhancements are particularly relevant at the CMF, Lovecraft, and L'Engle craters, which are of great interest because of the high density of radar-bright deposits, and where the USGS model mostly shows interpolated features. However, even for craters recognizable in the USGS map, results based on our SfS map are far more reliable in predicting shadowed areas and consistency with radar-bright regions.

While minor radar-bright spots (orange) closer to observation resolution might be related to our thresholding of the radar data, other residual radar-bright patches in our map may be due to inaccuracies in our SfS model, to subsurface ice, or to surface ice that survives very brief periods of direct illumination. Both targeted DEM improvement of PSRs and a more accurate study of the thermal environment in these regions would be necessary to get a full assessment of this matter. This is out of the scope of this work and the focus of ongoing and future analyses. However, our preliminary results highlight the increased predictive power of our new south pole DEM, allowing for a wide range of analyses to infer the physical characteristics of such near-surface deposits.

4. Conclusions and Future Work

Based on a selected subset of MESSENGER MDIS NAC images, we used the SfS routines provided by NASA ASP to produce an improved elevation model of Mercury's Southern hemisphere poleward of 75°S at a resolution of 250 m pix^{-1}. This is an unusually extensive application of `sfs`, for which we developed a custom set of tools and automated procedures to optimize image coverage and computational efficiency. Our new topography map enables the first detailed modeling of illumination near Mercury's south pole, as we extensively show in Section 3. Our highly resolved elevation models are a valuable resource for a future detailed modeling of both direct and scattered illumination, which is key in recovering variations in the surface albedo and surface composition. Modeling surface illumination also constitutes the first step toward retrieving the thermal evolution at or near the surface. In turn, knowledge of near-surface temperature over time is key to determining the nature of radar-bright deposits observed at Mercury poles (Harmon et al. 2011; Chabot et al. 2018), as previously shown at Mercury's north pole (Paige et al. 2013; Chabot et al. 2018b; Hamill et al. 2020; Barker et al. 2022; Gläser 2022). For instance, an accurate modeling of near-

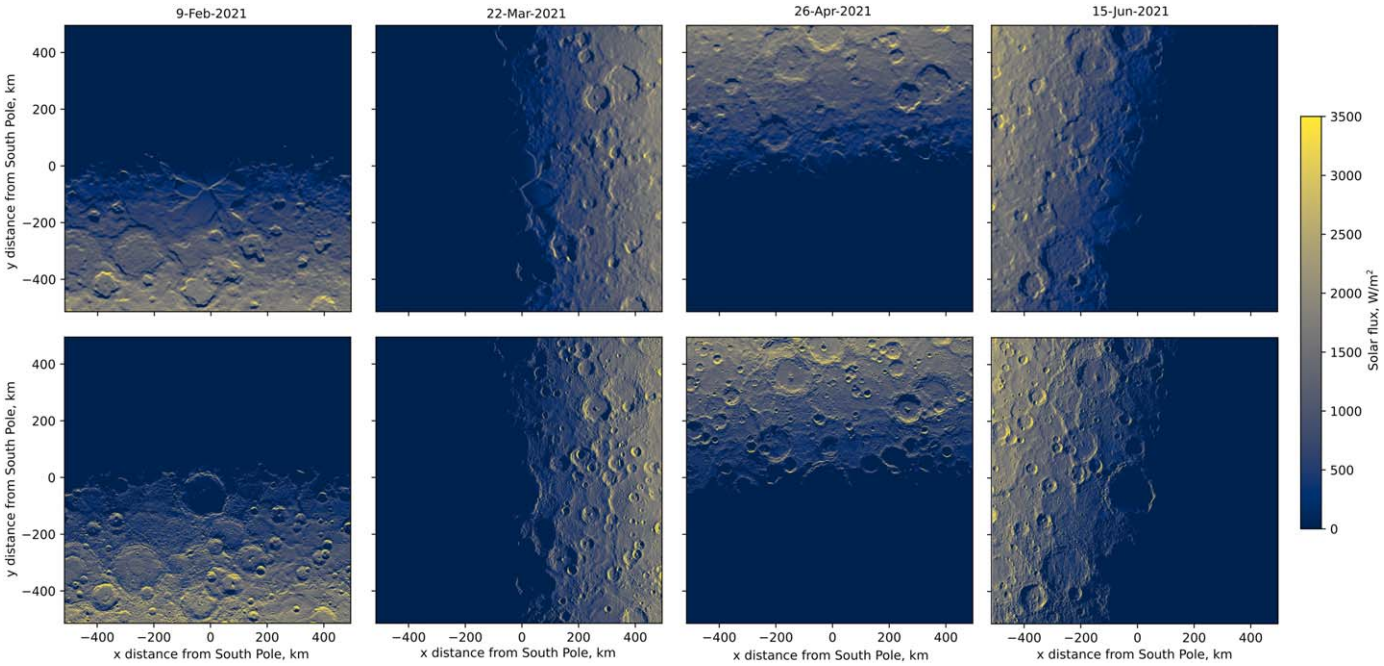

Figure 9. Rendering the USGS (top) and our DEM (bottom) with direct Sun illumination at noon of selected days covering a full Mercury solar cycle shows the increased level of detail of the recovered surface features and lack of large-scale artifacts when illuminating from any direction. Detailed simulations of time changing illumination are the basis to identify PSRs and cold regions, where ice and volatiles can persist.

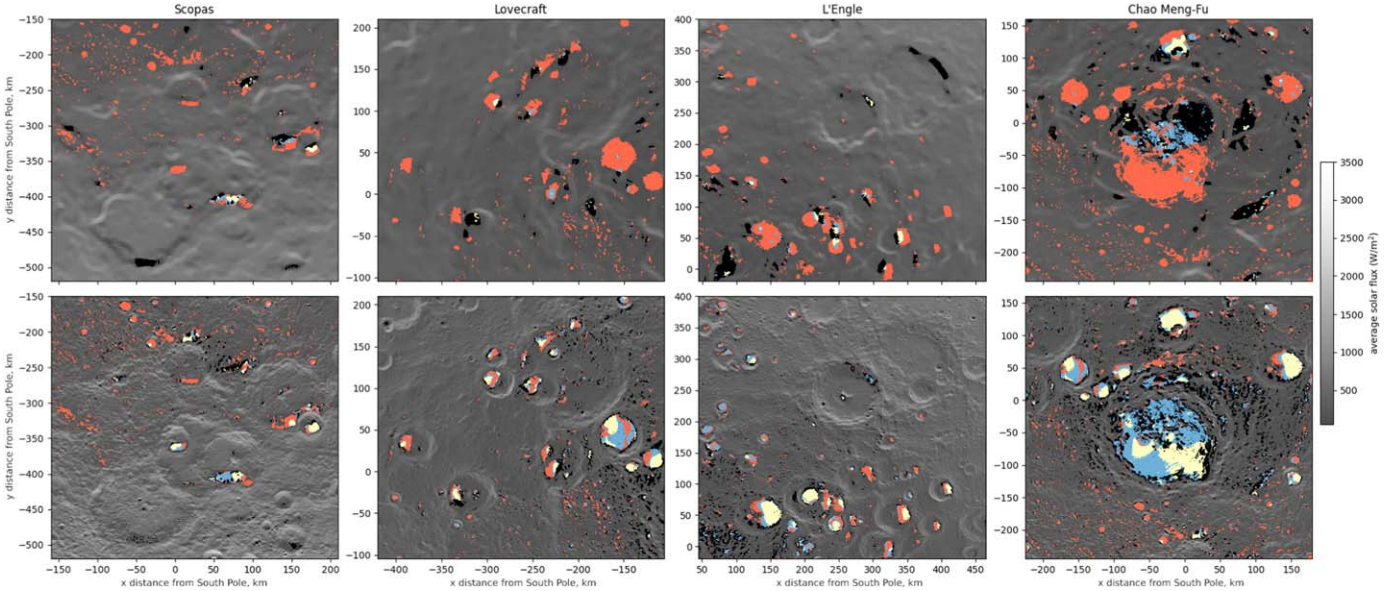

Figure 10. We show the average flux received at each south pole location over one solar cycle, according to the rendering of the USGS (top) and of our new DEM (bottom). We identify as PSRs the regions receiving an average <1 W m^{-2} (or <50 W m^{-2}, see below) over a solar cycle and we check consistency with persistently shadowed regions from Chabot et al. (2018). Most large PSRs coincide when evaluated with our DEM at <1 W m^{-2} (yellow) and <50 W m^{-2} (blue). PSRs identified by Chabot et al. (2018) but not by our renderings are shown in red, while rendered PSRs not expected by previous studies are shown in black: comparing the extent of such regions between our DEM (bottom) and the USGS DEM (top) highlights the improved strength of our model in predicting illumination conditions.

surface maximum and average temperature is necessary to assess whether water ice (or other volatiles) can survive near the surface over geological timescales.

Our results are thus a key step for advancing our knowledge of volatiles in Mercury's south polar region. In the context of this study, we presented a preliminary analysis by restricting ourselves to direct illumination of the surface by the Sun. This already shows promising results and an improved consistency between (cold) PSRs and high-reflectance potential ice and volatile deposits. In future work, we plan to leverage the increased resolution and level of detail provided by our new topographic model for the first comprehensive simulations of illumination and thermal conditions in Mercury's south polar region and to focus on placing constraints on the nature and history of volatiles on Mercury. While this work aimed at providing an improved terrain model for the whole south polar region, refined local solutions can be produced in the future for limited regions of high scientific interest to allow for a detailed study of volatile-rich craters. Indeed, potential users should be aware that our current model does not provide detailed terrain

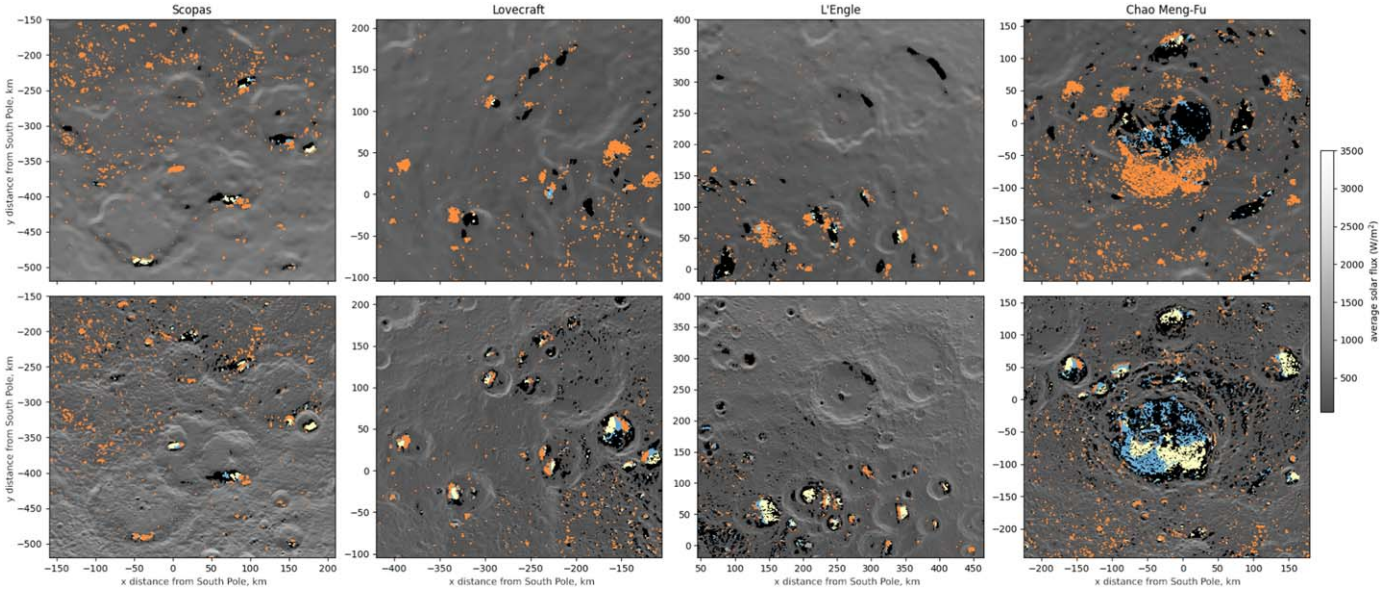

Figure 11. We show the average illumination received at each south pole location over one solar cycle, according to the rendering of the USGS (top) and of our new DEM (bottom). Most large radar-bright patches fall inside PSRs derived from our DEM with an average threshold flux of <1 W m^{-2} (yellow) or <50 W m^{-2} (blue). This is not the case for the USGS DEM (radar-bright spots marked as orange do not overlap rendered PSRs), highlighting the improved predicting power of our model.

elevation inside PSRs, which are not sampled by the MDIS NAC imagery. Moreover, improved models from this work are a valuable support for geological studies at Mercury's south pole, which has long been unsuited to e.g., geological tectonic structural mapping or photometric studies (e.g., Bernhardt & Clark 2022; Munaretto et al. 2023). The improved resolution and level of detail of our model will thus also support geological surveys in this region, by supplementing the analysis of MDIS images, where peculiar illumination conditions would hide features or introduce spurious artifacts.

While BepiColombo, and in particular the BepiColombo Laser Altimeter (Thomas et al. 2007) and the Spectrometer and Imaging for MPO BepiColombo Integrated Observatory SYStem (Cremonese et al. 2020) instruments, will in the future provide a first homogeneous mapping of both Mercury's hemisphere, the mission is still several years away from entering orbit and it is thus important to further exploit MESSENGER's extensive data sets to retrieve additional information about the planet, for both geophysical analysis, improving available a priori information, and supporting the preparation for the upcoming mission. Indeed, our work also has important implications for the planning of BepiColombo's observations, by allowing us to target the most interesting regions based on detailed and reliable simulations. We will be focusing on these aspects in upcoming publications.

S.B. acknowledges support by NASAs Planetary Science Division Research Program through the CRESST II cooperative agreement. S.B., E.M., and M.B. acknowledge support from the Planetary Geodesy Internal Scientist Funding Model work package funded by the NASA Planetary Science Division. The material is based upon work supported by NASA to S.B. under award No. 80GSFC21M0002. Support was provided by the NASA Discovery Data Analysis Program grant 80NSSC19K0881 to N.L.C. Resources supporting this work were provided by the NASA High-End Computing (HEC) Program through the NASA Center for Climate Simulation (NCCS) at Goddard Space Flight Center. Models and ancillary products resulting from this study will be available at the Planetary Geodesy Data Archive (https://pgda.gsfc.nasa.gov/) and doi:10.5281/zenodo.7542689.

ORCID iDs

Stefano Bertone https://orcid.org/0000-0001-9885-8440
Erwan Mazarico https://orcid.org/0000-0003-3456-427X
Michael K. Barker https://orcid.org/0000-0001-7980-2425
Matthew A. Siegler https://orcid.org/0000-0002-7940-3931
Jose M. Martinez-Camacho https://orcid.org/0000-0003-0542-7866
Colin D. Hamill https://orcid.org/0000-0002-9464-8494
Allison K. Glantzberg https://orcid.org/0000-0002-1929-8105
Nancy L. Chabot https://orcid.org/0000-0001-8628-3176

References

Alexandrov, O., & Beyer, R. A. 2018, E&SS, 5, 652
Bailen, M. B., Herkenhoff, K. E., Howington-Kraus, E. A., & Becker, K. J. 2015, LPSC, 46, 1074
Barker, M. K., Chabot, N. L., Mazarico, E., et al. 2022, PSJ, 3, 188
Barker, M. K., Mazarico, E., Neumann, G. A., et al. 2021, P&SS, 203, 105119
Barnouin, O. S., Daly, M. G., Palmer, E. E., et al. 2020, P&SS, 180, 104764
Becker, K. J., Robinson, M. S., Becker, T. L., et al. 2016, LPSC, 47, 2959
Benkhoff, J., van Casteren, J., Hayakawa, H., et al. 2010, P&SS, 58, 2
Bernhardt, H., & Clark, J. D. 2022, MExAG, 9040
Beyer, R., Alexandrov, O., McMichael, S., et al. 2021a, NeoGeographyToolkit/StereoPipeline 3.0.0 (3.0.0), Zenodo, doi:10.5281/zenodo.5140581
Beyer, R. A., Alexandrov, O., & McMichael, S. 2018, E&SS, 5, 537
Beyer, R. A., Alexandrov, O., & McMichael, S. 2021b, Ames Stereo Pipeline Documentation Release 3.0.0, https://github.com/NeoGeographyToolkit/StereoPipeline/releases/download/2023-01-17-daily-build/asp_book.pdf
2018, Blender Online Community Blender—a 3D modelling and rendering package, Blender Foundation, Stichting Blender Foundation, Amsterdam, http://www.blender.org
Chabot, N. L., Lawrence, D. J., Neumann, G. A., et al. 2018b, Mercury: The View after MESSENGER, ed. S. C. Solomon, L. R. Nittler, & B. J. Anderson (Cambridge: Cambridge Univ. Press), 346
Chabot, N. L., Shread, E. E., & Harmon, J. K. 2018, JGRE, 123, 666
Cremonese, G., Capaccioni, F., Capria, M. T., et al. 2020, SSRv, 216, 75
Deutsch, A. N., Chabot, N. L., Mazarico, E., et al. 2016, Icar, 280, 158

Fassett, C. I. 2016, P&SS, 134, 19
Fisher, E. A., Lucey, P. G., Lemelin, M., et al. 2017, Icar, 292, 74
Gaskell, R. W., Barnouin, O. S., Scheeres, D. J., et al. 2008, M&PS, 43, 1049
Glaser, P., Scholten, F., De Rosa, D., et al. 2014, Icar, 243, 78
Gläser, P. 2022, A&A, 664, A152
Gläser, P., & Gläser, D. 2019, A&A, 627, A129
Glaser, P., Oberst, J., Neumann, G. A., et al. 2018, P&SS, 162, 170
Hamill, C. D., Chabot, N. L., Mazarico, E., et al. 2020, PSJ, 1, 57
Harmon, J. K., Slade, M. A., & Rice, M. S. 2011, Icar, 211, 37
Hawkins, S. E., Boldt, J. D., Darlington, E. H., et al. 2007, SSRv, 131, 247
Horn, B. K. 1970, Shape From Shading: A Method For Obtaining The Shape Of A Smooth Opaque Object From One View, Tech. rep. 232, MIT Artificial Intelligence Laboratory, https://people.csail.mit.edu/bkph/AIM/AITR-232-OCR-OPT.pdf
Jorda, L., Gaskell, R., Capanna, C., et al. 2016, Icar, 277, 257
Landis, M. E., Hayne, P. O., Williams, J.-P., Greenhagen, B. T., & Paige, D. A. 2022, PSJ, 3, 39
Laura, J., Acosta, A., Addair, T., et al. 2022, Integrated Software for Imagers and Spectrometers 7.0.0, Zenodo, doi:10.5281/ZENODO.6950434
Mazarico, E., Barker, M. K., & Nicholas, J. B. 2018, AdSpR, 62, 3214
Mazarico, E., Rowlands, D. D., Neumann, G. A., et al. 2011, JGeod, 86, 193
McEwen, A. S. 1996, LPSC, 27, 841
Munaretto, G., Lucchetti, A., Pajola, M., Cremonese, G., & Massironi, M. 2023, Icar, 389, 115284
Neumann, G. A., Cavanaugh, J. F., Sun, X., et al. 2013, Sci, 339, 296
Paige, D. A., Siegler, M. A., Zhang, J. A., et al. 2010, Sci, 330, 479
Paige, D. A., Siegler, M. A., Harmon, J. K., et al. 2013, Sci, 339, 300
Perry, M. E., Neumann, G. A., Phillips, R. J., et al. 2015, GeoRL, 42, 6951
Potter, S. F., Bertone, S., Schörghofer, N., & Mazarico, E. 2022, JCPX, submitted (arXiv:2209.07632)
Preusker, F., Scholten, F., Matz, K. D., et al. 2016, NASA Planetary Data System, DAWN-A-FC2-5-VESTADTMSPG-V1.0, https://pds.nasa.gov/ds-view/pds/viewProfile.jsp?dsid=DAWN-A-FC2-5-VESTADTMSPG-V1.0
Preusker, F., Stark, A., Oberst, J., et al. 2018, LPICo, 2047, 6031
Rivera-Valentin, E. G., Meyer, H. M., Taylor, P. A., et al. 2022, PSJ, 3, 62
Rubanenko, L., Mazarico, E., Neumann, G. A., & Paige, D. A. 2018, JGRE, 123, 2178
Schorghofer, N., Mazarico, E., Platz, T., et al. 2016, GeoRL, 43, 6783
Schorghofer, N., Williams, J. P., Martinez-Camacho, J., Paige, D. A., & Siegler, M. A. 2021, GeoRL, 48, e95533
Siegler, M., Warren, P., Franco, K. L., et al. 2022, JGRE, 127, e07182
Smith, D. E., Zuber, M. T., Neumann, G. A., et al. 2017, Icar, 283, 70
Solomon, S. C., McNutt, R. L., Watters, T. R., et al. 2008, Sci, 321, 59
Susorney, H. C. M., Barnouin, O. S., Ernst, C. M., & Byrne, P. K. 2017, JGRE, 122, 1372
Susorney, H. C. M., Ernst, C. M., Chabot, N. L., Deutsch, A. N., & Barnouin, O. S. 2021, PSJ, 2, 97
2022, The CGAL Project CGAL User and Reference Manual, 5.5 ed. (CGAL Editorial Board), https://doc.cgal.org/latest/Manual/index.html
Thomas, N., Spohn, T., Barriot, J.-P., et al. 2007, P&SS, 55, 1398
Zuber, M. T., Smith, D. E., Phillips, R. J., et al. 2012, Sci, 336, 217